

# Forsterite dissolution and magnesite precipitation at conditions relevant for deep saline aquifer storage and sequestration of carbon dioxide

Daniel E. Giammar<sup>a,\*</sup>, Robert G. Bruant Jr.<sup>b</sup>, Catherine A. Peters<sup>b</sup>

<sup>a</sup>*Department of Civil Engineering and Environmental Engineering Science Program, Washington University, St. Louis, MO 63130, United States*

<sup>b</sup>*Program in Environmental Engineering and Water Resources, Department of Civil and Environmental Engineering, Princeton University, Princeton, NJ 08544, United States*

Received 30 April 2003; accepted 10 December 2004

---

## Abstract

The products of forsterite dissolution and the conditions favorable for magnesite precipitation have been investigated in experiments conducted at temperature and pressure conditions relevant to geologic carbon sequestration in deep saline aquifers. Although forsterite is not a common mineral in deep saline aquifers, the experiments offer insights into the effects of relevant temperatures and  $P_{\text{CO}_2}$  levels on silicate mineral dissolution and subsequent carbonate precipitation. Mineral suspensions and aqueous solutions were reacted at 30 °C and 95 °C in batch reactors, and at each temperature experiments were conducted with headspaces containing fixed  $P_{\text{CO}_2}$  values of 1 and 100 bar. Reaction products and progress were determined by elemental analysis of the dissolved phase, geochemical modeling, and analysis of the solid phase using scanning electron microscopy, infrared spectroscopy, and X-ray diffraction. The extent of forsterite dissolution increased with both increasing temperature and  $P_{\text{CO}_2}$ . The release of Mg and Si from forsterite was stoichiometric, but the Si concentration was ultimately controlled by the solubility of amorphous silica. During forsterite dissolution initiated in deionized water, the aqueous solution reached supersaturated conditions with respect to magnesite; however, magnesite precipitation was not observed for reaction times of nearly four weeks. Magnesite precipitation was observed in a series of experiments with initial solution compositions that simulated extensive forsterite dissolution. The precipitation of magnesite appears to be limited by the process of nucleation, and nucleation requires a critical saturation index between 0.25 and 1.14 at 95 °C and 100 bar  $P_{\text{CO}_2}$ . Magnesite precipitation is fastest in the presence of an initial magnesite seed. Although magnesite precipitates do form on the surfaces of forsterite particles, the presence of the forsterite surface does not significantly accelerate magnesite precipitation relative to solid-free systems.

© 2005 Elsevier B.V. All rights reserved.

*Keywords:* Carbon dioxide; Dissolution; Forsterite; Magnesite; Precipitation; Sequestration

---

\* Corresponding author. Fax: +1 314 935 5464.

*E-mail address:* degiammar@seas.wustl.edu (D.E. Giammar).

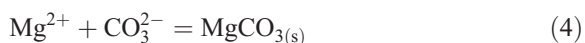
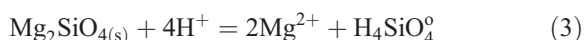
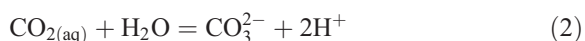
## 1. Introduction

Anthropogenic perturbations of the global carbon cycle over the last two centuries have led to the accumulation of CO<sub>2</sub> in the atmosphere. The recent increases in atmospheric CO<sub>2</sub> have exerted a discernible influence on global climate, and numerous models predict even more significant climate change in the decades to come (Albritton and Meira Filho, 2001). The transformation of CO<sub>2</sub> to dissolved bicarbonate ions during silicate mineral weathering has long been considered an important sink for atmospheric CO<sub>2</sub> in models of the natural global carbon cycle on geological time-scales (Kump et al., 2000; Press and Siever, 1998). Interactions of CO<sub>2</sub> with silicate minerals can also play a significant role in strategies for mitigating the atmospheric accumulation of CO<sub>2</sub> on much shorter time-scales.

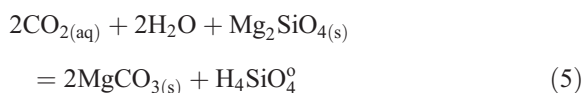
Separation and subsequent storage of CO<sub>2</sub> is one method of mitigating emissions. Deep saline aquifers are a prime candidate for CO<sub>2</sub> storage because of their large potential storage capacity and their occurrence in many of the same sedimentary basins where fossil fuels are found (Bachu, 2000; Bruant et al., 2002). The fate of carbon injected into deep saline aquifers as supercritical CO<sub>2</sub> will be governed by its physical properties and interactions with the formation water and aquifer mineralogy. Mechanisms of storing and sequestering CO<sub>2</sub> in aquifers can be categorized as 1) stratigraphic trapping: the physical isolation of CO<sub>2</sub> beneath a confining aquitard, 2) solubility trapping: the dissolution of CO<sub>2</sub> in the aqueous phase, 3) hydrodynamic trapping: the inhibition of migration of dissolved CO<sub>2</sub> due to slow flow of aquifer fluids, and 4) mineral trapping: the precipitation of carbonate minerals as a result of dissolved CO<sub>2</sub> interactions with aquifer minerals and dissolved solids (Bachu, 2000; Bachu et al., 1996).

Mineral trapping requires the participation of cations, including Ca<sup>2+</sup>, Fe<sup>2+</sup>, and Mg<sup>2+</sup>, that can form stable solid carbonate phases. These cations may be initially present in the aqueous solution or may result from the dissolution of silicate minerals. An example of a mineral trapping mechanism is illustrated in Eqs. (1)–(5) using forsterite as an example Mg-rich silicate mineral. The reactions of CO<sub>2</sub> dissolution in water (1), carbonic acid formation and

deprotonation (2), forsterite dissolution (3), and magnesite precipitation (4),



yield a net mineral trapping reaction (5):



It is important to note that while net reaction (5) is thermodynamically favorable under the pressure and temperature conditions of interest, the extent of product formation depends on the rates of the preceding four reactions.

Although uncommon in saline aquifers, olivines are useful model minerals for the study of mineral dissolution and carbonate precipitation at high temperature and CO<sub>2</sub> conditions because their dissolution is relatively rapid and generally stoichiometric (Chen and Brantley, 2000; Rosso and Rimstidt, 2000; Westrich et al., 1993; Wogelius and Walther, 1991) and because they have a high potential for mineral carbonate formation (Goff and Lackner, 1998; Xu et al., 2001). Numerous studies of forsterite dissolution at ambient and some non-standard conditions (Blum and Lasaga, 1988; Chen and Brantley, 2000; Goff and Lackner, 1998; Oelkers, 2001; Pokrovsky and Schott, 2000b; Rosso and Rimstidt, 2000; Westrich et al., 1993; Wogelius and Walther, 1991; Xu et al., 2001) provide reference information against which effects of high temperature and CO<sub>2</sub> may be compared.

Mineral trapping (Eq. (5)) is generally considered to be a slow process that is limited by the rates of silicate mineral dissolution and carbonate mineral precipitation. Until recently, experimental investigations of silicate mineral reaction at conditions similar to those of CO<sub>2</sub> injection in saline aquifers have not observed the precipitation of carbonate minerals for reaction times as long as 30 days (Gunter et al., 1996; Sass et al., 2001). A recent investigation of the

reaction of shale and arkose materials in CO<sub>2</sub>–brine systems at 200 °C and 200 bar for 80 days resulted in the precipitation of magnesite, analcime (NaAlSi<sub>2</sub>O<sub>6</sub>·H<sub>2</sub>O), and clays (Kaszuba et al., 2003). Modeling has enabled the simulation of reactions that may occur on time-scales longer than those of experiments. Reactive transport and batch models of active and proposed CO<sub>2</sub> injection projects in deep saline aquifers predict the formation of magnesite, dawsonite (NaAl(CO<sub>3</sub>)<sub>2</sub>) (Johnson et al., 2002; Johnson et al., 2001), and siderite (Gunter et al., 2000; Xu et al., 2001) following CO<sub>2</sub> injection. In addition to in situ mineral trapping in aquifers, mineral carbonation in engineered reactors offers another method for converting CO<sub>2</sub> into a stable solid phase. Mineral carbonation involves the reaction of minerals rich in Mg, Ca, or Fe(II) in high-CO<sub>2</sub> aqueous systems to yield carbonate minerals. Unaltered dunites, which are composed primarily of olivine, are considered the optimal feed materials for mineral carbonation (Goff and Lackner, 1998). Magnesite has been formed from serpentine and olivine in stirred autoclave reactors (Guthrie et al., 2001; O'Connor et al., 2002).

Magnesite precipitation requires the development of supersaturated solution compositions, which can be generated by the neutralization of carbonic acid by forsterite dissolution (Eqs. (2)–(3)). Precipitation is initiated by nucleation of a solid phase, and subsequent precipitation occurs as crystal growth. The degree of supersaturation is described in terms of either the magnesite saturation ratio ( $\Omega$ ) or saturation index (SI), and these values are defined in terms of the magnesite solubility product ( $K_{sp}$ ) and the ion activity product (IAP) as defined in Eqs. (6a–d).

$$K_{sp} = \{Mg^{2+}\}_{eq} \{CO_3^{2-}\}_{eq} \quad (6a)$$

$$IAP = \{Mg^{2+}\}_{act} \{CO_3^{2-}\}_{act} \quad (6b)$$

$$\Omega = \frac{IAP}{K_{sp}} \quad (6c)$$

$$SI = \log \Omega \quad (6d)$$

The subscripts “eq” and “act” refer to equilibrium and actual, respectively. The activities of dissolved

ions  $\{i\}$  are the products of their molar concentrations  $[i]$  and activity coefficients  $\gamma_i$ . Nucleation may occur homogeneously in solution or heterogeneously at a mineral–water interface. The onset of nucleation, the nucleation rate, and subsequent crystal growth are all influenced by the degree of supersaturation (Lasaga, 1998).

This study investigated the dissolution of forsterite and precipitation of magnesite at conditions relevant to deep saline aquifer carbon storage and sequestration. The primary objectives of the study were the characterization of secondary phases that result from forsterite reaction and the identification of critical supersaturation conditions and nucleating surfaces favorable for magnesite nucleation and growth. The investigation of forsterite dissolution at these extreme conditions also extends the range of conditions previously studied and provides a model system for evaluating the effects of deep saline aquifer conditions on mineral dissolution processes. The objectives were addressed in a series of batch reaction experiments with aqueous mineral suspensions performed at constant temperature under a CO<sub>2</sub> headspace. Reaction progress and secondary phase precipitation were investigated by combining elemental analysis of the dissolved phase with characterization of reacted and unreacted solid phases.

## 2. Experimental materials and methods

### 2.1. Materials

Forsterite from San Carlos, Arizona was obtained from Ward's Scientific. The initial material was crushed to a size of about 1 mm and the purest crystals were selected by visual inspection. The composition of this material is Fo<sub>89</sub> (Mg<sub>1.78</sub>Fe<sub>0.22</sub>SiO<sub>4</sub>) as determined by X-ray fluorescence (XRF), X-ray diffraction (XRD), and digestion, which is consistent with compositions determined in previous studies. The material was further crushed in an alumina dish-and-puck crusher and sieved to segregate a 125–250 μm size fraction. A portion of the initial forsterite was also crushed to a finer size range of 20–50 μm based on differential settling in a column of water. The size fraction from settling is nominal because aggregates of particles smaller than 20 μm were also selected in this

process. Prior to use in experiments, a suspension of the 125–250  $\mu\text{m}$  forsterite was sonicated and allowed to settle to remove any very fine particles. After size separation and washing, all size fractions were air dried at room temperature and stored in the dry atmosphere of a bench-top dessicator. The surface area of the sonicated and size-separated 20–50  $\mu\text{m}$  material was determined to be  $15.0 \pm 0.03 \text{ m}^2 \text{ g}^{-1}$  by BET- $\text{N}_2$  adsorption (Brunauer et al., 1938), and a surface area of  $0.088 \text{ m}^2 \text{ g}^{-1}$  was estimated for the 125–250  $\mu\text{m}$  material based upon a published correlation of grain-size versus specific surface area that was developed from multiple BET measurements by  $\text{N}_2$  and Kr adsorption for forsteritic olivine (Brantley and Mellott, 2000). A small amount of synthetic magnesite was prepared by reacting a solution of  $\text{MgCl}_2$  and  $\text{NaHCO}_3$  at  $95^\circ\text{C}$  and 100 bar  $P_{\text{CO}_2}$ . The synthesized material was identified as magnesite by XRD. Approximately 20  $\mu\text{m}$  rhombohedral magnesite crystals, frequently intergrown, were observed by scanning electron microscopy.

Solutions of  $\text{MgCl}_2$  and  $\text{NaHCO}_3$  were prepared by dissolution of crystalline solids. All solutions were prepared with ultrapure (18.2 M $\Omega$  cm) water from a point-of-use purification system (Millipore). Solid carbon dioxide (i.e., dry ice) was used to generate carbon dioxide pressures in batch reactors. Calibration standards for inductively coupled plasma optical emission spectrometry analysis were prepared from standard solutions of Mg, Fe, and Si (SPEX CertiPrep, Inc.).

## 2.2. Experimental procedure

Batch reactions were performed in 23 mL Teflon-lined vessels of stainless steel acid digestion bombs (Parr Instrument Company). Teflon is a porous material, and so before adding the reactants, the reactors were loaded with only dry ice and held at the desired temperature in order to saturate the pore spaces. As much as 1.4 g of carbon dioxide could be taken up by the Teflon vessels. The pre-conditioned vessels were opened and weighed empty. Reactant solutions, which had been flash frozen by immersion in liquid nitrogen, were then added to the reactors and weighed. For experiments with mineral solids, pre-weighed portions of the solid were added to the reactors. In all experiments, except those with synthetic magnesite, the solids were added to yield

concentrations in suspension of  $20 \text{ g L}^{-1}$ . Pre-weighed portions of dry ice were added to the reactors, and the reactors were then quickly sealed and brought to the desired temperature in either an oven or temperature-controlled water bath. The reactors were weighed once a day to monitor for loss of carbon dioxide due to leakage. The only mixing that the reactors received was an inversion during the daily weighing process. At the conclusion of experiments, sealed reactors were weighed and then cooled in a freezer for less than 1 h before opening. Once reactors were opened, dissolved phase samples were collected with plastic syringes, filtered through 0.22  $\mu\text{m}$  syringe filters (Millipore), and then acidified with nitric acid to either 2% or 5% by volume. The remaining solids were washed out of the reactors, filtered with 0.2  $\mu\text{m}$  filter membranes, air-dried at room temperature, and stored prior to analysis. The empty reactors were dried and reweighed for comparison with the initial empty reactor masses.

While the temperature ( $T$ ) of the reactor was controlled by the oven or water bath, the pressure was controlled by the headspace of  $\text{CO}_2$ . By using solid carbon dioxide to generate the partial pressure of  $\text{CO}_2$ , the total pressure ( $P$ ) is the sum of contributions of the initial ambient atmosphere and the pressure generated from the phase change of the  $\text{CO}_2$ . In the 100 bar experiments, the total pressure was nearly equivalent to the  $P_{\text{CO}_2}$ . The actual pressure in a reactor was calculated from the known volume of the reactor ( $V_T$ ) and the measured mass of  $\text{CO}_2$  according to Eqs. (7a–c), in which  $m_{\text{CO}_2}$ ,  $m_{\text{CO}_2,\text{w}}$ , and  $m_{\text{CO}_2,\text{f}}$  are the masses of total, dissolved, and separate phase  $\text{CO}_2$  respectively.

$$m_{\text{CO}_2} = m_{\text{CO}_2,\text{w}} + m_{\text{CO}_2,\text{f}} \quad (7a)$$

$$m_{\text{CO}_2,\text{w}} = [\text{H}_2\text{CO}_3^*] V_{\text{soln}} \text{MW}_{\text{CO}_2} \quad (7b)$$

$$m_{\text{CO}_2,\text{f}} = \left( V_T - \frac{m_{\text{soln}}}{\rho_{\text{soln}}(P, T, I)} - \frac{m_{\text{mineral}}}{\rho_{\text{mineral}}} \right) \rho_{\text{CO}_2}(P, T) \quad (7c)$$

In Eqs. (7b) and (7c),  $m_{\text{soln}}$  and  $m_{\text{mineral}}$  are the masses of the aqueous solution and minerals initially present,  $\rho_{\text{soln}}$  and  $\rho_{\text{mineral}}$  are their densities,  $\text{MW}_{\text{CO}_2}$  and  $\rho_{\text{CO}_2}$  are the molecular weight and density of  $\text{CO}_2$ , and

$V_{\text{soln}}$  is the volume of the aqueous solution. The value of  $\rho_{\text{soln}}$  was calculated as a function of pressure, temperature, and ionic strength ( $I$ ) according to published equations (Batzle and Wang, 1992) and does not attempt to account for changes in the solution density that would result from  $\text{CO}_2$  dissolution. The concentration of  $\text{H}_2\text{CO}_3^*$  ( $[\text{H}_2\text{CO}_{3(\text{aq})}] + [\text{CO}_{2(\text{aq})}]$ ) was calculated as a function of pressure, temperature, and ionic strength using recently published equations (Duan and Sun, 2003). The density and fugacity of  $\text{CO}_2$  in the headspace were determined using published equations of state (Sterner and Pitzer, 1994). The pressure that satisfies Eqs. (7a–c) was found by iterative calculation. For use in the equations for  $\rho_{\text{soln}}$  and  $[\text{H}_2\text{CO}_3^*]$ , the ionic strength was converted to an

equivalent molality of NaCl. Calculated pressures were validated in a series of tests conducted using a reactor with a pressure gauge. The pressures within the reactors decreased in several experiments as a result of  $\text{CO}_2$  leakage, which was determined by monitoring changes in  $m_{\text{CO}_2}$  over the course of an experiment as measured by changes to the total reactor mass.

Forsterite dissolution experiments were performed in dilute solution at 30 °C or 95 °C and approximately 1 or 100 bar  $P_{\text{CO}_2}$  for reaction times as long as 629 h. The conditions of all batch experiments conducted are presented in Table 1. Magnesite precipitation experiments were designed to evaluate the effects of the presence of an initial solid, reaction time, and the

Table 1  
Batch experiments performed

Experiment	Starting solid	Aqueous composition	$I_{\text{max}}^{\text{a}}$ (M)	$T$ (°C)	$P_{\text{CO}_2}^{\text{b}}$ (bar)	pH		$\text{SI}_{\text{init}}$ magnesite	Duration (h)
						Initial	Final <sup>c</sup>		
<i>Forsterite dissolution experiments</i>									
D1	FO <sub>89</sub> 125–250 μm	DI H <sub>2</sub> O	0.003	30	1	3.92	5.03	N/A	24, 73, 174
D2	FO <sub>89</sub> 125–250 μm	DI H <sub>2</sub> O	0.006	30	38–103	3.11	3.58	N/A	25, 72, 169, 629
D3	FO <sub>89</sub> 125–250 μm	DI H <sub>2</sub> O	0.009	95	1	4.15	6.07	N/A	26, 74, 170
D4	FO <sub>89</sub> 125–250 μm	DI H <sub>2</sub> O	0.018	95	82–97	3.22	4.73	N/A	25, 73, 176, 630
D5	FO <sub>89</sub> 20–50 μm	DI H <sub>2</sub> O	0.063	95	87–104	3.22	4.97	N/A	8, 25, 72, 168, 335
<i>Magnesite precipitation experiments</i>									
P1	FO <sub>89</sub> 125–250 μm	0.01 M MgCl <sub>2</sub> + 0.02 M NaHCO <sub>3</sub>	0.07	95	94–96	4.59	4.85	–0.43	240
P2	FO <sub>89</sub> 125–250 μm	0.02 M MgCl <sub>2</sub> + 0.04 M NaHCO <sub>3</sub>	0.12	95	85–91	4.86	5.03	0.25	240
P3	FO <sub>89</sub> 125–250 μm	0.05 M MgCl <sub>2</sub> + 0.10 M NaHCO <sub>3</sub>	0.25	95	85–97	5.21	5.32	1.14	240
P4	FO <sub>89</sub> 125–250 μm	0.10 M MgCl <sub>2</sub> + 0.20 M NaHCO <sub>3</sub>	0.51	95	84–96	5.49	5.55	1.85	240
P5	FO <sub>89</sub> 125–250 μm	0.15 M MgCl <sub>2</sub> + 0.30 M NaHCO <sub>3</sub>	0.75	95	86–95	5.66	5.69	2.27	240
P6	FO <sub>89</sub> 125–250 μm	0.25 M MgCl <sub>2</sub> + 0.50 M NaHCO <sub>3</sub>	1.25	95	70–108	5.89	5.48	2.80	336
P7–P9	none, synthetic magnesite, FO <sub>89</sub> 20–50 μm	0.15 M MgCl <sub>2</sub> + 0.30 M NaHCO <sub>3</sub>	0.75	95	80–97	5.66	5.37–5.67	2.27	240
P10–P12	FO <sub>89</sub> 125–250 μm	0.15 M MgCl <sub>2</sub> + 0.30 M NaHCO <sub>3</sub>	0.75	95	88–103	5.66	5.57–5.69	2.27	68, 240, 377

<sup>a</sup> The maximum ionic strength ( $I_{\text{max}}$ ) is calculated from the solution composition. For dissolution experiments,  $I_{\text{max}}$  is achieved at the longest reaction time. For precipitation experiments,  $I_{\text{max}}$  is either the initial  $I$  if Mg is lost from solution during the reaction or the  $I$  at the end of the experiment if Mg is released to solution during the reaction.

<sup>b</sup> The  $P_{\text{CO}_2}$  decreases over the course of an experiment due to  $\text{CO}_2$  leakage from the batch reactor.

<sup>c</sup> The final pH value is given for the experiment with the longest duration.

initial magnesite saturation index. Precipitation experiments were conducted in the presence of forsterite from both the 125–250  $\mu\text{m}$  and 20–50  $\mu\text{m}$  size fractions, synthetic magnesite, and in the absence of solid. The effect of reaction time on magnesite precipitation was investigated using a set of reactors containing 125–250  $\mu\text{m}$  forsterite and an initial magnesite saturation index of 2.27. Note that forsterite dissolution (Eq. (3)) results in elevated concentrations of  $\text{Mg}^{2+}$  and  $\text{H}_4\text{SiO}_{4(\text{aq})}$  and also in the production of alkalinity (i.e., the consumption of  $\text{H}^+$ ). Selected solution compositions of  $\text{MgCl}_2$  and  $\text{NaHCO}_3$  were chosen to simulate extensive forsterite dissolution.

### 2.3. Analytical methods

Aqueous samples were analyzed for total dissolved Mg, Si, and Fe using a PerkinElmer Optima 4300DV inductively coupled plasma optical emission spectrometer. X-ray diffraction analyses were performed with a Scintag PAD V system with  $\text{CuK}\alpha$  radiation and an Ortec GLP photon detector. Samples for XRD analysis included 10% by mass silicon metal as an internal standard. Scanning electron microscopy images were collected with a Philips XL30 FEG-SEM equipped with a PGT-IMIX PTS dispersive X-ray system for elemental analysis. Infrared spectra were collected using a Bruker IFS 66 V/S FTIR instrument with a mid-IR source and liquid-nitrogen cooled MCT detector. Solid samples for FTIR analysis were prepared by grinding the solid sample with KBr to a very fine powder and were analyzed with a Harrick Seagull diffuse reflectance (DRIFTS) accessory. Surface areas were determined by the  $\text{N}_2$  adsorption/BET method on a Micromeritics ASAP 2010 instrument. X-ray fluorescence analysis was performed by a commercial laboratory (ALS Chemex).

### 2.4. Equilibrium modeling of speciation

Geochemical equilibrium modeling was used to calculate the pH and magnesite saturation indices of the solutions in the batch reactors. The pH of a system was calculated using the pressure, temperature, ionic strength, and the total dissolved concentrations of Mg and Si. In situ measurements of pH were not possible in the experiments because all reactions were carried

out in completely sealed Teflon vessels. Modeling was performed using the chemical equilibrium software program MINEQL+Version 4.5 (Schecher and McAvoy, 1998). Input files were altered to incorporate equilibrium constants for the conditions of 95 °C and 100 bar and to set  $[\text{H}_2\text{CO}_3^*]$  to the fixed value determined by the reactor temperature, pressure, and ionic strength (Table 2). The value for  $[\text{H}_2\text{CO}_3^*]$  was

Table 2  
Equilibrium constants for relevant reactions at experimental conditions

	log $K$ (°C, bar $P_{\text{CO}_2}$ ) <sup>a</sup> , $I=0$ M		log $K'$ (°C, bar $P_{\text{CO}_2}$ ), $I=0.5$ M NaCl <sup>b</sup>
	(25, 1)	(95, 100)	(95, 100)
<i>Dissolved phase reactions</i>			
$\text{H}_2\text{CO}_3^*$ (M) fixed by $T$ and $P_{\text{CO}_2}$ <sup>c</sup>	0.032	0.784	0.719
$\text{H}_2\text{O}=\text{H}^++\text{OH}^-$	–14.00	–12.30	–11.95
$\text{CO}_{2(\text{aq})}+\text{H}_2\text{O}=\text{HCO}_3^-+\text{H}^+$	–6.35	–6.32	–5.97
$\text{CO}_{2(\text{aq})}+\text{H}_2\text{O}=\text{CO}_3^{2-}+2\text{H}^+$	–16.67	–16.36	–15.30
$\text{SiO}_{2(\text{aq})}+\text{H}_2\text{O}=\text{HSiO}_3^-+\text{H}^+$	–9.59	–8.95	–8.60
$\text{Mg}^{2+}+\text{H}_2\text{O}=\text{MgOH}^++\text{H}^+$	–11.68	–9.53	–9.89
$\text{Mg}^{2+}+\text{H}^++\text{CO}_3^{2-}=\text{MgHCO}_3^+$	11.37	11.41	–10.00
$\text{Mg}^{2+}+\text{CO}_3^{2-}=\text{MgCO}_3(\text{aq})$	2.98	3.44	2.03
$\text{Mg}^{2+}+\text{SiO}_{2(\text{aq})}+\text{H}_2\text{O}=\text{MgHSiO}_3^++\text{H}^+$	–8.33	–7.53	–7.88
<i>Solubility reactions</i>			
$\text{SiO}_{2(\text{amorphous})}=\text{SiO}_{2(\text{aq})}$	–2.71	–2.19	–2.19
$\text{Mg}(\text{OH})_{2(\text{s})}+2\text{H}^+=\text{Mg}^{2+}+2\text{H}_2\text{O}$	16.30	12.67	13.46
$\text{Mg}_2\text{SiO}_4(\text{s})+4\text{H}^+=2\text{Mg}^{2+}+\text{SiO}_{2(\text{aq})}+2\text{H}_2\text{O}$	27.89	20.91	21.62
$\text{MgCO}_3(\text{s})=\text{Mg}^{2+}+\text{CO}_3^{2-}$	–8.04	–9.31	–7.90

<sup>a</sup> All values, except  $\text{CO}_{2(\text{aq})}$ , were calculated using SUPCRT92 with the slop98 database.

<sup>b</sup>  $K'$  is the conditional equilibrium constant based on concentrations of species and is specific to a particular ionic strength. Activity coefficients were calculated with the Davies Equation.

<sup>c</sup>  $\text{H}_2\text{CO}_3^*=\text{H}_2\text{CO}_3+\text{CO}_{2(\text{aq})}$ . Concentration is a fixed value that is in equilibrium with a headspace at a fixed  $P_{\text{CO}_2}$ . Calculations were made using the equations of state of (Sterner and Pitzer, 1994) and the solubility equations of (Duan and Sun, 2003).

calculated as described previously by using published equations for CO<sub>2</sub> fugacity (Sterner and Pitzer, 1994) and solubility (Duan and Sun, 2003). Equilibrium constants at non-standard temperature and pressure were determined using the SUPCRT92 software package (Johnson et al., 1992) with the slop98 thermodynamic datafile. Activity coefficients to account for the effects of ionic strength were calculated with the Davies Equation (Davies, 1962), which includes two temperature-dependent constants. Values specific to 95 °C were determined within MINEQL+. The Davies Equation has a useful range of 0–0.5 M, which includes the conditions of most of the experiments (Table 1). For experiments with higher ionic strength solutions, a value of 0.5 M was used for calculating activity coefficients and these calculations are considered to be less reliable than those for more dilute conditions.

### 3. Results

#### 3.1. Forsterite dissolution

Fig. 1 shows the cumulative release of Mg and Si for four dissolution experiments (experiments D1–

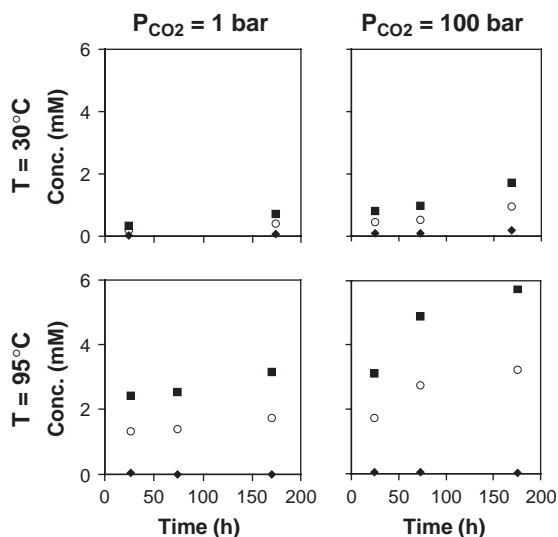


Fig. 1. Dissolved concentrations of Mg (■), Si (○), and Fe (◆), during batch dissolution of 20 g L<sup>-1</sup> Fo<sub>89</sub> in dilute solution (experiments D1–D4).

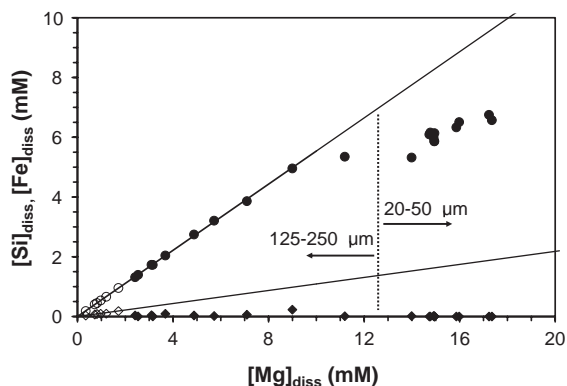


Fig. 2. Dissolved concentrations of Si (●, ○) and Fe (◆, ◇) versus the dissolved Mg concentration for all batch dissolution experiments conducted with 20 g L<sup>-1</sup> Fo<sub>89</sub> in dilute solution. Data are included for experiments with both the coarse (125–250 μm) and fine (20–50 μm) size fractions at temperatures of 95 °C (closed symbols) and 30 °C (open symbols). Lines representing the stoichiometric ratios for perfectly congruent dissolution of Mg<sub>1.78</sub>Fe<sub>0.22</sub>SiO<sub>4</sub> are included for reference.

D4) at two temperatures (30 °C and 95 °C) and two  $P_{\text{CO}_2}$  levels (1 bar and 100 bar). The overall extent of dissolution increases with both increasing temperature and  $P_{\text{CO}_2}$ . The increased extent of reaction with increasing  $P_{\text{CO}_2}$  is most likely dominated by the effect of decreasing pH with increasing  $P_{\text{CO}_2}$  ( $\text{pH}_{\text{init}}=4.15$  at 1 bar and  $\text{pH}_{\text{init}}=3.22$  at 100 bar for 95 °C), although there may also be an independent effect of increasing the total pressure. An experiment with the higher surface area 20–50 μm material (experiment D5) resulted in faster and more extensive dissolution than with the 125–250 μm material.

Mineral dissolution is considered to be congruent if elements are released at the stoichiometric ratios of the dissolving mineral. Fig. 2 plots the measured concentrations of dissolved Si and Fe versus the dissolved Mg concentration. Lines representing the stoichiometric ratios in the forsterite are included for reference. Fe release was stoichiometric only at 30 °C. At 95 °C dissolved Fe concentrations were well below stoichiometric concentrations, which suggests that either released Fe was taken up by the precipitation and growth of a secondary solid phase or that forsterite dissolution is incongruent with preferential release of Mg relative to Fe. Iron(III) oxide and oxyhydroxide minerals are the most likely Fe-containing secondary precipitates to have formed. The

solution conditions of all of the experiments with data shown in Fig. 2 are highly supersaturated with respect to goethite (saturation indices >3.7) and hematite (saturation indices >8.2). Only two of the experiments were mildly supersaturated with respect to siderite (saturation indices <0.4) and no experiments were saturated with respect to Fe(II) silicates. Si release from the solid phase was perfectly congruent in all experiments when Si concentrations were below 5 mM. Experiments with concentrations greater than 5 mM were those conducted for long reaction times and/or with the high surface area 20–50  $\mu\text{m}$  forsterite. As with Fe release, a sub-stoichiometric release of Si suggests the incorporation of released Si in a secondary solid phase. The characterization and identification of potential secondary phases is discussed below and in the Discussion.

Reaction path trajectories were calculated for forsterite dissolution at the experimental conditions and were compared with experimental results. Fig. 3 presents the predicted reaction paths together with the data from dissolution experiments conducted at

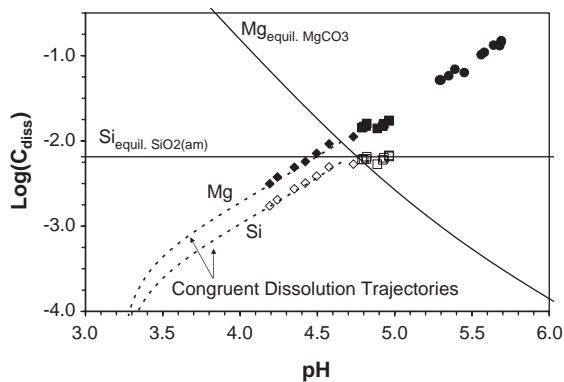


Fig. 3. The  $\text{Mg}_2\text{SiO}_4\text{-CO}_2\text{-H}_2\text{O}$  system at 95 °C and 100 bar  $P_{\text{CO}_2}$ . Solid lines are the calculated values of dissolved Mg and Si as a function of pH as controlled by equilibrium with magnesite and amorphous silica. The dotted lines are calculated reaction paths for the congruent dissolution of forsterite. Measured concentrations of dissolved Mg (closed symbols) and Si (open symbols) are included from the dissolution experiments with forsterite from the 125–250  $\mu\text{m}$  (◆, ◇) and 20–50  $\mu\text{m}$  (■, □) size fractions and from magnesite precipitation experiments (●) in which magnesite precipitation was verified. While the equilibrium lines and reaction trajectories were plotted for the ideal conditions of 100 bar  $P_{\text{CO}_2}$  and dilute solution, the data points are plotted at the measured dissolved concentration and the calculated pH value for the ionic strength and  $P_{\text{CO}_2}$  of the actual experiment.

95 °C and 100 bar  $P_{\text{CO}_2}$  (experiments D4–D5). As forsterite dissolves, Mg and Si are released to solution and  $\text{H}^+$  is consumed. The pH can be calculated by applying mass and charge balance to the system for conditions of fixed  $P_{\text{CO}_2}$  and total dissolved Mg and Si concentrations. Mg and Si concentrations will increase until they are limited by the solubility of secondary solid phases, which are expected to be magnesite and amorphous silica, respectively. While Si concentrations increased until they stabilized near the line for  $\text{SiO}_{2(\text{am})}$  solubility, Mg concentrations reached levels that exceeded predicted magnesite solubility. Magnesite saturation indices as high as 0.25 were achieved without magnesite precipitation.

Dissolution of forsterite at 95 °C and 100 bar  $P_{\text{CO}_2}$  resulted in the extensive formation of etch pits as seen in the scanning electron micrographs in Fig. 4. In addition to etch pit formation, agglomerates of fine-grained Fe-rich material were observed in the proximity of etch pits. Energy-dispersive X-ray (EDX) analyses show that the secondary material was substantially enriched in Fe and O relative to forsterite. At the macroscopic level, the formation of a secondary phase was indicated by a very noticeable change in color from pale green for unreacted forsterite to reddish-brown for reacted material. Neither XRD nor DRIFTS analysis could detect this secondary phase. Non-detection suggests that the secondary iron-rich phase was either not present at an amount sufficient for detection or that it was amorphous and/or did not contain functional groups that are IR active over the wavenumber range analyzed. The formation of the secondary iron-rich phase was unique to the 95 °C experiments and was not observed visually or with SEM–EDX for the 30 °C experiments.

### 3.2. Magnesite precipitation

Fig. 5 shows the changes in solution composition and reactor conditions with time for forsterite reaction starting at initial conditions that were supersaturated for magnesite (experiments P10–P12). The dissolved Si concentration increased approximately linearly with time, while the Mg concentration decreased with time and the rate of decrease accelerated. The increasing Si concentration indicates that forsterite was dissolving

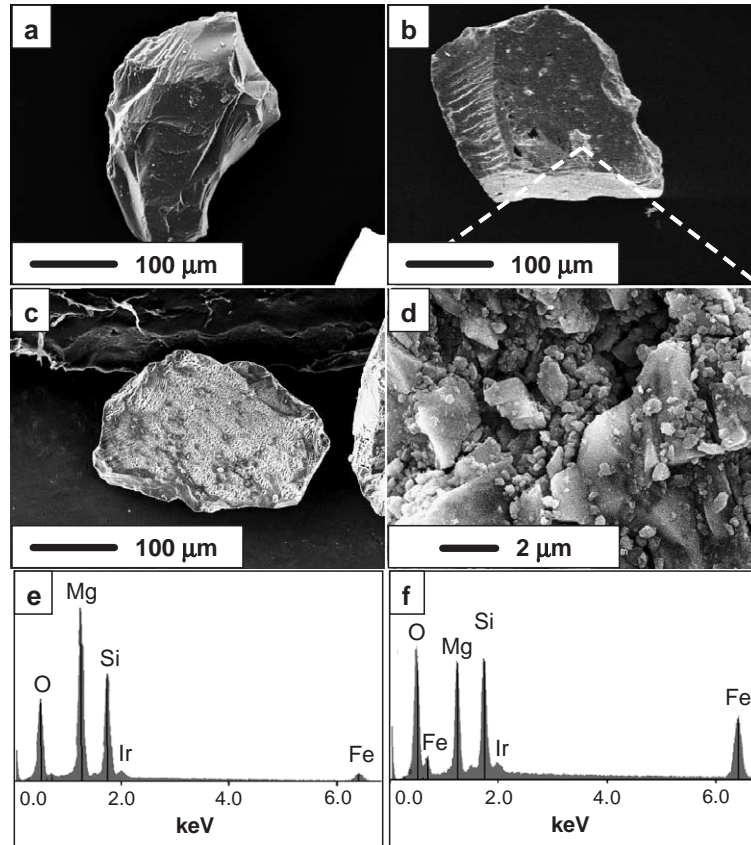


Fig. 4. Scanning electron micrographs of unreacted forsterite (a) and forsterite reacted for 73 h (b) and 176 h (c) at 95 °C and 100 bar  $P_{\text{CO}_2}$  in dilute solution. A precipitate cluster in the lower central portion of the particle reacted for 73 h is shown at higher magnification (d). Energy-dispersive X-ray analysis of the cluster shows that it is enriched in Fe and O (f) relative to unreacted forsterite (e). The iridium peak in the EDX spectra is the result of sample coating for imaging.

even as magnesite was precipitating. The relatively high  $\text{NaHCO}_3$  concentration buffers the pH at 5.6–5.7, which is in contrast to the large changes in pH in the unbuffered forsterite dissolution experiments.

Decreasing dissolved Mg concentrations provide macroscopic evidence of magnesite precipitation. Fig. 6a shows dissolved Mg concentrations as a function of initial saturation index (experiments P1–P6), and Fig. 6b shows Mg concentrations in the presence of different solid phases (experiments P7–P9). The amount of Mg precipitated on a mole basis ( $n_{\text{Mg,ppt}}$ ) was determined as:

$$n_{\text{Mg,ppt}} = \left( [\text{Mg}]_{\text{diss,init}} + [\text{Mg}]_{\text{diss,Fo}} - [\text{Mg}]_{\text{diss,fin}} \right) \times V_{\text{soln}} \quad (8)$$

where  $[\text{Mg}]_{\text{diss,init}}$  and  $[\text{Mg}]_{\text{diss,fin}}$  are the initial and final dissolved Mg concentrations respectively. The Mg released by forsterite dissolution ( $[\text{Mg}]_{\text{diss,Fo}}$ ) can be calculated from the final dissolved Si concentration and by assuming congruent dissolution (Eq. (9)).

$$[\text{Mg}]_{\text{diss,Fo}} = 1.78[\text{Si}]_{\text{diss,fin}} \quad (9)$$

At saturation indices of 1.14 and less,  $[\text{Mg}]_{\text{diss,init}}$  was nearly identical to the sum of  $[\text{Mg}]_{\text{diss,init}}$  and  $[\text{Mg}]_{\text{diss,Fo}}$ , which provided no evidence for magnesite precipitation. Magnesite precipitation was evident from macroscopic observations only for initial saturation indices of 1.85 and higher. In evaluating the effect of initial solid, the most extensive removal of

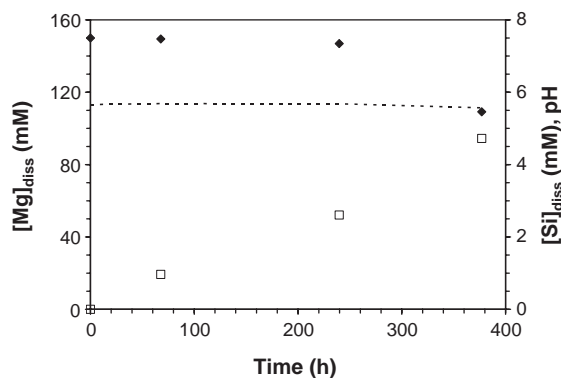


Fig. 5. Reaction of 20 g L<sup>-1</sup> forsterite (125–250 μm fraction) at 95 °C and 100 bar  $P_{\text{CO}_2}$  from an initial solution of 0.15 M MgCl<sub>2</sub> and 0.30 M NaHCO<sub>3</sub> (experiments P10–P12). Dissolved concentrations of Mg (◆) and Si (□) indicate the precipitation of magnesite and dissolution of forsterite respectively. The equilibrium pH (---) is determined from  $P_{\text{CO}_2}$  and solution composition.

magnesium from solution was in the presence of synthetic magnesite. There was little difference between magnesium precipitation in systems with no initial solid and those with 125–250 μm forsterite. More magnesium precipitated with the 20–50 μm fraction of forsterite (15 m<sup>2</sup> g<sup>-1</sup>) than with the 125–250 μm size fraction (0.088 m<sup>2</sup> g<sup>-1</sup>), suggesting that the extent of precipitation increased with the available surface area.

At the initiation of each precipitation experiment, magnesite was the only solid for which the solution was supersaturated because no Si had yet been released from the dissolution of forsterite; however, at the final conditions of several of the precipitation experiments, the aqueous phase was supersaturated with respect to magnesium silicates as well as magnesite. The final solution compositions of experiments P3–P6, P9, and P11–12 were supersaturated with respect to talc (saturation indices of 0.75 to 4.19), and the final solution composition of experiment P9 was also supersaturated with respect to chrysotile (saturation index=0.39). Despite the supersaturation of the solutions with respect to solids other than magnesite, magnesite was the only phase initially at supersaturation and analyses of the reacted solids (presented below) only provide evidence for the presence of magnesite.

XRD analysis confirmed that the Mg-containing solid that precipitated in the reactors was magnesite

(Fig. 7). Magnesite reflections (32.6°, 35.9°, and 45.0°) are only clearly seen in the diffraction pattern for the reaction conducted at the highest saturation index (2.80) and may be present at 32.6° as a shoulder on a forsterite peak in the pattern for an initial saturation index of 2.27. Assuming that all Mg precipitated from solution was present in magnesite, the relative fractions of magnesite and forsterite can be calculated on a mass basis. The

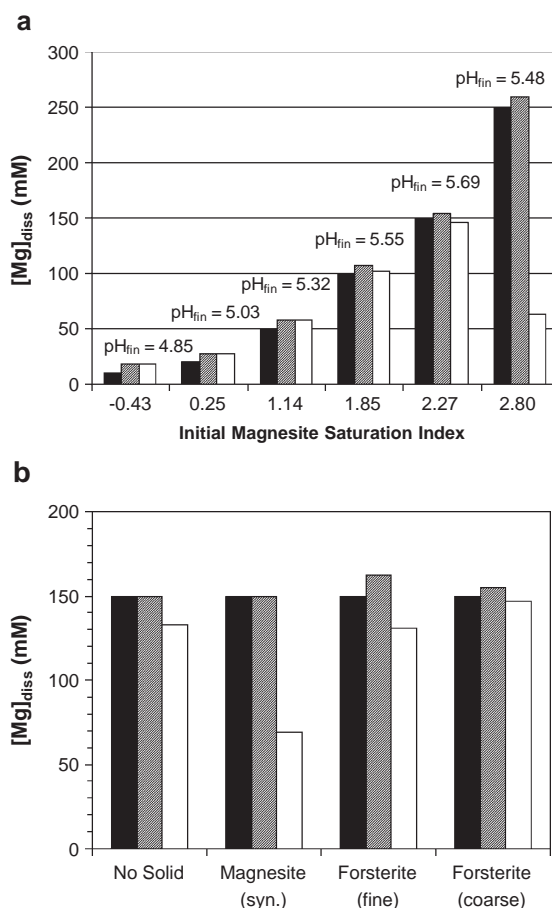


Fig. 6. Dissolved Mg concentrations before (■) and after (□) batch reactions at 95 °C and 100 bar  $P_{\text{CO}_2}$  with a) 20 g L<sup>-1</sup> forsterite (125–250 μm fraction) and different initial magnesite saturation indices (experiments P1–P6) and b) in the presence of different initial solids at an initial magnesite saturation index of 2.27 (experiments P5, P7–P9). The middle column corresponds to the sum of the initial Mg concentration and the Mg released from forsterite dissolution as determined from the dissolved Si concentration and assuming congruent dissolution.

solids from the experiment with the highest initial saturation index (experiment P6) were 45.2% magnesite on a mass basis and those from the experiment with the next highest initial saturation index (experiment P5) were 3.5% magnesite, which appears to be close to the detection limit for magnesite using XRD.

Infrared spectroscopy was employed as another method of detecting and characterizing carbonate species (sorbed or precipitated). The DRIFTS spectra of a series of samples reacted at varying initial saturation indices (experiments P3–P6) are presented in Fig. 8. The spectra of magnesite include peaks resulting from the out-of-plane  $\text{CO}_3^{2-}$  bend ( $\nu_2$ ) at 855 and 899  $\text{cm}^{-1}$ , the asymmetric  $\text{CO}_3^{2-}$  stretch at 1457  $\text{cm}^{-1}$ , and an unidentified vibration at 1825  $\text{cm}^{-1}$ . The forsterite spectrum is characterized by the triply degenerate asymmetric stretch of  $\text{SiO}_4^{4-}$  ( $\nu_3$ ) at 835, 889, and 979  $\text{cm}^{-1}$ . The magnesite spectrum can only be resolved from the forsterite spectrum for a saturation index of 2.27 and higher, suggesting that DRIFTS requires about 3.5% magnesite by mass for detection.

The spatial distribution and extent of the precipitates identified as magnesite by XRD and DRIFTS were investigated using SEM–EDX. In experiments conducted for 240 and 336 h at different initial saturation indices in the presence

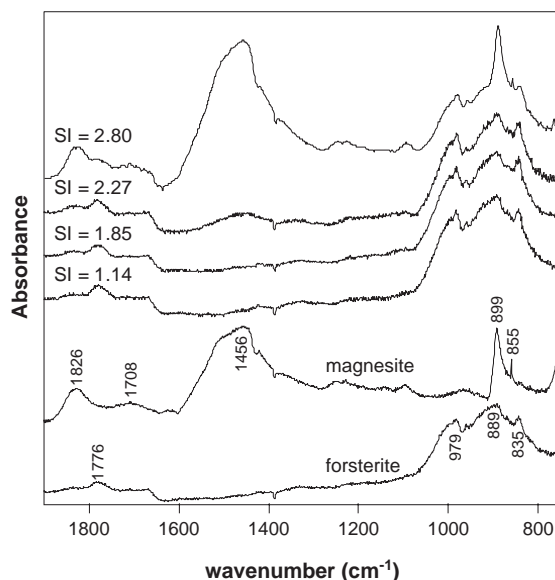


Fig. 8. DRIFTS spectra of solids from 240 h (experiments P3–P5) and 336 h (experiment P6) experiments at 95 °C and 100 bar  $P_{\text{CO}_2}$  with solutions of varying initial saturation indices for magnesite. The spectra of unreacted forsterite and pure synthetic magnesite are shown for reference.

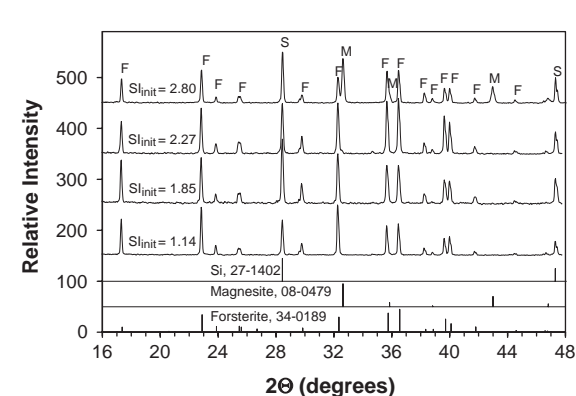


Fig. 7. X-ray diffraction patterns of solids from 240 h (experiments P3–P5) and 336 h (experiment P6) experiments at 95 °C and 100 bar  $P_{\text{CO}_2}$  with solutions of varying initial saturation indices for magnesite. Reference patterns are given for forsterite, magnesite, and silicon metal, which was used as an internal standard. In the top pattern, the dominant peaks are labeled for either forsterite (F), silicon (S), or magnesite (M).

of 125–250  $\mu\text{m}$  forsterite (experiments P1–P6), magnesite precipitates associated with forsterite surfaces were observed for saturation indices of 1.14 and higher (Fig. 9). The abundance and size of the magnesite crystals increased with increasing magnesite saturation. Magnesite occurred as discrete crystals associated with the forsterite surface, suggesting growth from initial nucleation sites on the forsterite surface. The magnesite crystals grew as large as 10  $\mu\text{m}$  and are distinguished not only based on their morphology but also by their distinctive EDX spectra (Fig. 9). SEM was also used to observe the precipitation of magnesite on forsterite particles with increasing time in solutions with an initial saturation index of 2.27 (Fig. 10). After just 68 h, initial magnesite precipitation was seen with SEM (Fig. 10b), which corresponds to a time when macroscopic analyses (Fig. 5) still show little change in the Mg concentration. The rhombohedral crystal observed in Fig. 10b was determined to be magnesite by its morphology and Mg-rich composition as determined by EDX; the composition of the very fine-grained material on the surface is unknown. After 240 and 377 h of reaction, larger

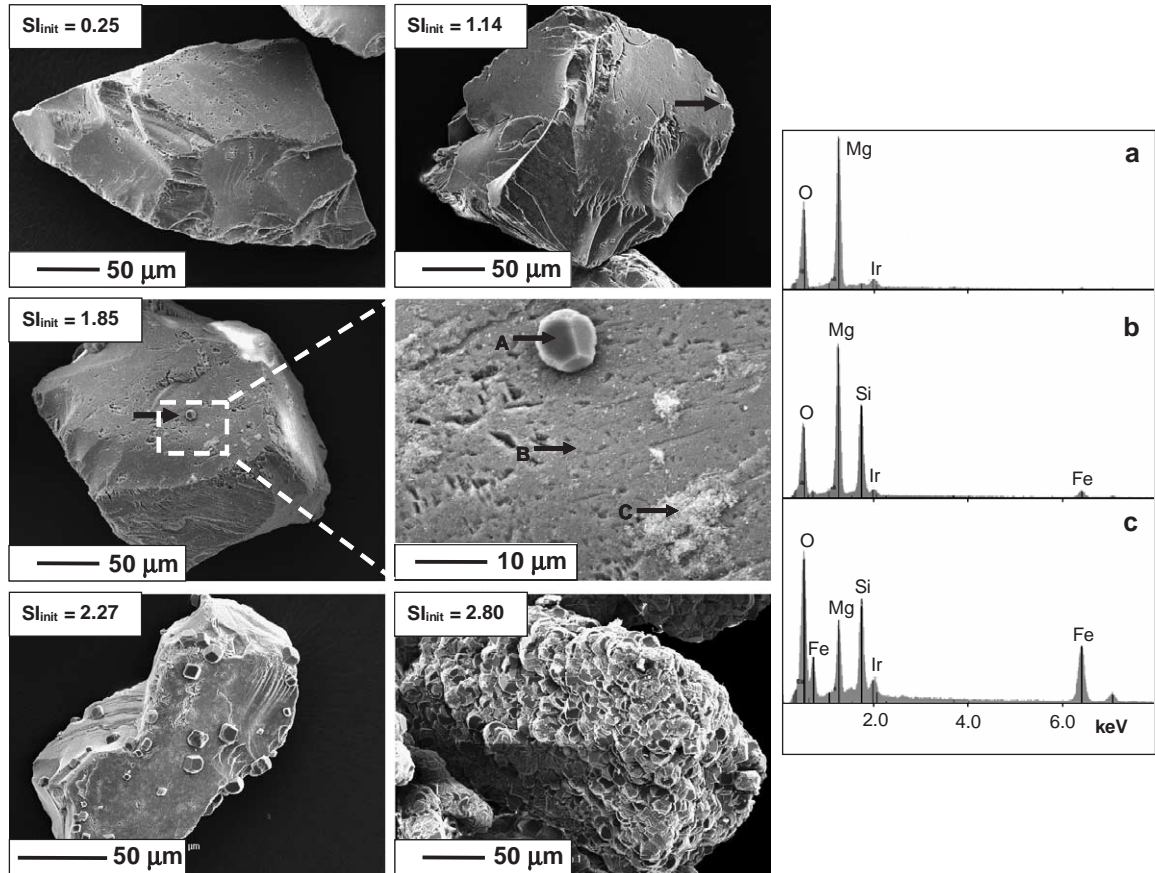


Fig. 9. Scanning electron micrographs of forsterite reacted for 240 h (experiments P2–P5) and 336 h (experiment P6) at 95 °C and 100 bar  $P_{\text{CO}_2}$  with solutions of varying initial saturation indices for magnesite. No magnesite is observed in the experiment with an initial index of 0.25, and arrows identify magnesite crystals in images with low amounts of precipitation. The magnesite precipitate that formed in the experiment with a saturation index of 1.85 is shown at higher magnification, and the energy-dispersive X-ray spectra for spot analyses of this sample show characteristic spectra of the unaltered forsterite surface (a), magnesite (b), and an iron-rich secondary phase (c). The iridium peak in the EDX spectra is the result of sample coating for imaging.

magnesite crystals had formed and the nucleation of new crystals had occurred.

#### 4. Discussion

##### 4.1. Stoichiometry of forsterite dissolution and precipitation of secondary phases

The stoichiometry of elemental release during forsterite dissolution in deionized water is determined by 1) the congruency of the dissolution process and 2) the formation of secondary and/or altered surface phases. For forsterite dissolution initiated in deionized

water, Mg released to solution was conserved in the dissolved phase because no Mg-containing secondary phases formed. Consequently, Mg can serve as a reference for Si and Fe behavior. The evolution of dissolved Si concentrations followed the stoichiometric Si:Mg ratio at both 30 °C and 95 °C when Si concentrations were below the solubility limit of amorphous silica. Dissolved Fe concentrations followed the stoichiometric Fe:Mg ratio only at 30 °C, and Fe concentrations were very sub-stoichiometric at 95 °C.

The stoichiometric release of Mg and Si observed in the present work is consistent with previous observations of congruent forsterite dissolution over

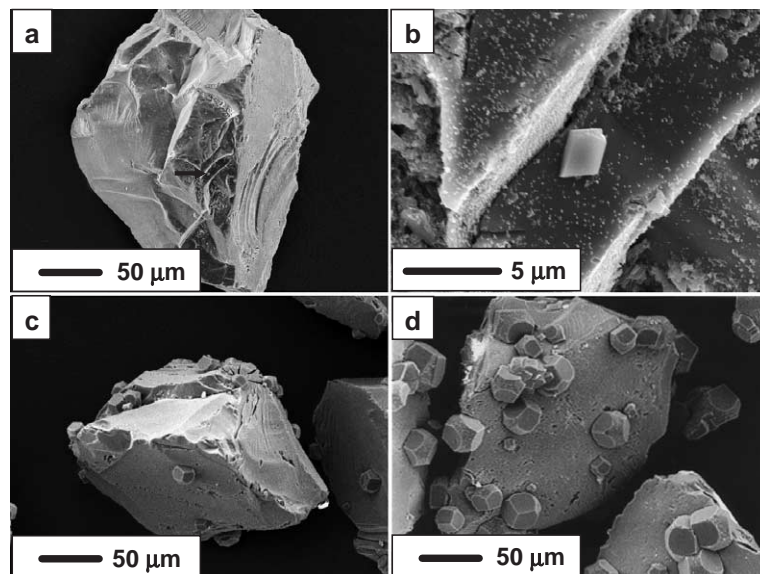


Fig. 10. Scanning electron micrographs of forsterite with precipitated magnesite following reaction for 68 (a), 240 (c), and 377 (d) h at 95 °C and 100 bar  $P_{\text{CO}_2}$  with an initial solution of 0.15 M  $\text{MgCl}_2$  and 0.30 M  $\text{NaHCO}_3$  ( $\text{SI}_{\text{init}}=2.27$ ) (experiments P10–P12). A small magnesite particle that formed after 68 h is identified with an arrow and shown at higher magnification (b).

a similar pH range (Rosso and Rimstidt, 2000; Westrich et al., 1993; Wogelius and Walther, 1991). Macroscopic observations of congruent dissolution are also consistent with mechanistic interpretations of forsterite dissolution. In acidic solutions, the protonation of surface sites is considered the first step in the dissolution process. Oelkers (Oelkers, 2001) suggested that following a limited extent of rapid proton exchange for Mg, protonation of a Mg octahedron weakens the chain-linking Mg–O–Mg bonds to adjacent octahedra, which allows for simultaneous release of Mg and Si from the structure. Pokrovsky and Schott (Pokrovsky and Schott, 2000b) also suggested that  $\text{H}^+$  exchange for Mg is rapid, and that the rate controlling surface complex is a Si dimer formed by polymerization of two silica surface sites.

Ratios of Si:Mg that are lower than stoichiometric were observed for the most extensive forsterite dissolution, which can be interpreted as the precipitation of amorphous silica following congruent dissolution. Precipitation was suggested by the clustering of dissolved Si concentrations at the equilibrium solubility of amorphous silica (Fig. 3). Substoichiometric Si:Mg ratios would also result from preferential release of Mg, but previous studies have only observed preferential Mg release during the

initial phases of forsterite dissolution (Luce et al., 1972; Oelkers, 2001; Pokrovsky and Schott, 2000a). No direct observations of amorphous silica were made during analysis of the reacted solids using SEM–EDX, XRD, and DRIFTS, which can be explained by the low mass concentration of amorphous silica in the reacted solids and its inherently amorphous nature. It may also be possible that Si was retained in the solid phase in a Si-rich surface layer. Investigations using X-ray photoelectron spectroscopy have observed a surface enrichment of Si for the orthosilicates forsterite, fayalite ( $\text{Fe}_2\text{SiO}_4$ ), and tephroite ( $\text{Mn}_2\text{SiO}_4$ ) (Pokrovsky and Schott, 2000b; Rodrigues et al., 1998; Seyama et al., 1996; Westrich et al., 1993); however, any Si-rich surface layer was quite thin with an estimated thickness of only 10–20 Å (Pokrovsky and Schott, 2000b) and studies using infrared spectroscopy, secondary ion mass spectrometry (Luce et al., 1972), and transmission electron microscopy (Westrich et al., 1993) found no Si-rich surface layer.

The observed non-stoichiometric release of Fe at 95 °C most likely resulted from the oxidation of Fe(II) to Fe(III) and the subsequent precipitation of Fe(III) oxide or oxyhydroxide phases. The aqueous solutions of the experiments were supersaturated with respect to hematite and goethite as well as other Fe(III) oxy-

hydroxide solids. The oxidation of Fe(II) may either occur at the surface of the dissolving solid or in solution following the release of Fe(II) from forsterite. The formation of clusters of Fe-rich particles is consistent with oxidation in solution, and the proximity of the clusters to dissolution etch pits suggests that oxidation was rapid and the residence time of Fe(II) in solution was very short. While Fe(II) oxidation is thermodynamically favorable over a wide pH range, including that of the current study, it may be kinetically hindered at low pH where the thermodynamics are less favorable (Stumm and Morgan, 1996). The kinetic inhibition of Fe(II) oxidation explains the stoichiometric Fe release at 30 °C, and the increase in temperature to 95 °C is sufficient to overcome the activation energy barrier. Chen and Brantley (2000) have made a similar observation of substoichiometric release of Fe during forsterite dissolution at 65 °C and pH>4. The formation of a Fe(III)-containing surface phase may inhibit subsequent dissolution at long reaction times (Chen and Brantley, 2000; Wogelius and Walther, 1992); however, a recent study found that a porous iron-rich surface coating did not inhibit the dissolution of anorthite (Hodson, 2003).

#### 4.2. Trends in forsterite dissolution rate

While the focus of the present work is on the secondary phases formed in forsterite–CO<sub>2</sub>–H<sub>2</sub>O systems, evaluation of dissolution rates can be made for comparison with previous studies. The dissolution rates of minerals can be interpreted within the framework of a general rate law (Eq. (10)) that incorporates the effects of temperature, catalyzing or inhibiting species, and reaction affinity (Lasaga, 1995; Lasaga, 1998).

$$\text{Rate} = k_0 e^{\frac{-E_a}{RT}} \prod_i \{i\}^{n_i} f(\Delta G) \quad (10)$$

The rate is expressed in terms of mol cm<sup>-2</sup> s<sup>-1</sup>,  $k_0$  is a dissolution rate constant,  $E_a$  is the apparent activation energy [J mol<sup>-1</sup>],  $\{i\}$  expresses the activity of inhibiting or catalyzing species  $i$  [M],  $n_i$  is the reaction order for the species, and  $\Delta G$  is the overall Gibbs free energy change for the dissolution reaction [J mol<sup>-1</sup>]. Assuming a particular form of the dependence on reaction affinity (i.e., Gibbs free energy

change) and considering only the catalyzing or inhibiting effects of H<sup>+</sup>, Eq. (10) simplifies to Eq. (11), where  $n$  is an adjustable constant ( $n=1$  for an elementary reaction).

$$\text{Rate} = k_0 e^{\frac{-E_a}{RT}} \{H^+\}^{n_{H^+}} \left(1 - e^{\frac{n\Delta G}{RT}}\right) \quad (11)$$

Because forsterite is highly soluble at ambient surface conditions and those of the batch reactors, the reaction of forsterite dissolution is always very far from equilibrium (i.e.,  $\Delta G$  with respect to forsterite dissolution is very negative) and Eq. (11) can be simplified further (Eq. (12)). A lack of dependence of the forsterite dissolution rate on dissolved concentrations of Mg and Si has been experimentally verified (Oelkers, 2001; Rosso and Rimstidt, 2000).

$$\text{Rate} = k_0 e^{\frac{-E_a}{RT}} \{H^+\}^{n_{H^+}} \quad (12)$$

It should be noted that the term for the temperature dependence is an apparent activation energy because the dissolution of a mineral is not a single elementary reaction but rather a complex series of reactions, each with its own activation energy (Lasaga, 1995; Lasaga, 1998).

The effect of  $P_{\text{CO}_2}$  on the extent of forsterite dissolution (Fig. 1) can be qualitatively interpreted using the dissolution rate law of Eq. (12). Current experiments show that the extent of dissolution after a fixed period of time, which reflects the average dissolution rate, increased with increasing  $P_{\text{CO}_2}$ . The effect of increasing  $P_{\text{CO}_2}$  was most likely the indirect result of the decrease in pH that occurs as  $P_{\text{CO}_2}$  increases. A reaction order of approximately 0.5 with respect to H<sup>+</sup> activity at acid to neutral pH is widely established for forsterite (Blum and Lasaga, 1988; Rosso and Rimstidt, 2000; Wogelius and Walther, 1991; Wogelius and Walther, 1992), and a similar reaction order ( $0.45 \pm 0.1$ ) was observed for an entire series of orthosilicates (Casey and Westrich, 1992; Westrich et al., 1993). The variation of the dissolution rate with pH has been interpreted as the variation of forsterite surface speciation with pH (Blum and Lasaga, 1988; Pokrovsky and Schott, 2000a). At neutral and acid pH, several studies have seen no direct effect of CO<sub>2</sub> on the dissolution rates of silicate

and aluminosilicate minerals. The dissolution rates of augite and anorthite at pH 4 were independent of  $P_{\text{CO}_2}$  from ambient to 1 atm (Brady and Carroll, 1994). At pH 3.2 and temperatures from 30 to 100 °C, no effect of  $P_{\text{CO}_2}$  variation from ambient to 95 atm was observed for labradorite dissolution rates (Carroll and Knauss, 2001). Similarly the dissolution rates of volcanic ash soils at pH 2.8–4.0 and 22 °C were unaffected by  $P_{\text{CO}_2}$  variation from ambient to 1 atm (Stephens, 2002; Stephens and Hering, 2004). However, there may be direct effects of  $P_{\text{CO}_2}$  at higher pH conditions where the carbonate ion is dominant. At basic pH conditions, both an inhibition of forsterite (Pokrovsky and Schott, 2000a; Pokrovsky and Schott, 2000b; Wogelius and Walther, 1991) and diopside (Knauss et al., 1993) dissolution and a possible enhancement of anorthite dissolution (Berg and Banwart, 2000) have been observed with increasing  $P_{\text{CO}_2}$ .

The observed increase in the extent of forsterite dissolution with increasing temperature can also be interpreted by Eq. (12). As the temperature increases, the Arrhenius term in Eq. (12) dictates an increase in dissolution rate at constant pH, and the magnitude of this effect is determined by the apparent activation energy. There is considerable variation in published values of the apparent activation energy for forsterite dissolution, which may be explained by considering the pH-dependence of the apparent activation energy. At acidic to neutral pH, a marked decrease of the apparent activation energy with increasing pH has been observed (Chen and Brantley, 2000; Rosso and Rimstidt, 2000; Westrich et al., 1993). Over a pH range of 1.8 to 6.0, estimates of the apparent activation energy for forsterite dissolution range from 42.6 to 63.8 kJ mol<sup>-1</sup> (Oelkers, 2001; Rosso and Rimstidt, 2000; Westrich et al., 1993).

During forsterite dissolution in dilute solution, the rate of release of elements to solution decreased as the reaction progressed (Fig. 1). The initial period of rapid dissolution may be due to the preferential dissolution of fine particles, mineral coatings, or highly reactive sites. In the dissolution experiments initiated in deionized water, the pH was not constant but instead increased as the forsterite dissolved, which may also explain the decreasing dissolution rate. When the pH was held constant, as in experiments buffered at pH 5.6–5.7 with NaHCO<sub>3</sub> (experiments P10–P12,) the

release of Si from forsterite dissolution was approximately linear with respect to time (Fig. 5). The dissolution rate calculated from this linear release of Si with time is  $1.9 \times 10^{-13}$  mol cm<sup>-2</sup> s<sup>-1</sup>. Applying the rate equation of Rosso and Rimstidt (Rosso and Rimstidt, 2000) to the conditions of experiments P10–P12 predicts a rate of  $4.7 \times 10^{-12}$  mol cm<sup>-2</sup> s<sup>-1</sup>. The rate calculated with the Rosso and Rimstidt equation may be higher than the current rate determination because the experimental reactors were only intermittently mixed and also because the activation energy may be lower at pH 5.6 than at the conditions for which Rosso and Rimstidt developed their rate equation.

#### 4.3. Magnesite precipitation

Despite conditions of magnesite supersaturation with a saturation index as high as 0.25, magnesite precipitation did not occur following the dissolution of forsterite in dilute solution. Assuming the thermodynamic data used to estimate magnesite solubility are accurate, the lack of magnesite precipitation suggests that the formation of magnesite is kinetically hindered and supersaturated conditions may persist without magnesite precipitation. The precipitation of a solid phase consists of the two separate processes of nucleation and growth. If nucleation is the rate-limiting step, then precipitation will not occur until conditions are sufficiently supersaturated to initiate nucleation. The accelerating Mg loss from solution during magnesite precipitation (Fig. 5) is consistent with nucleation as the rate-limiting step. Following an initially slow decrease in the Mg concentration that is limited by nucleation, magnesite precipitation accelerates as magnesite crystals grow (Fig. 10). Further evidence for nucleation as the rate-limiting step is provided by the comparison of magnesite precipitation in the presence of different initial solids. After 240 h of reaction, magnesite precipitation was much greater in the system seeded with magnesite than in systems seeded with other solids (Fig. 6b). Precipitation in the system with magnesite started as growth, but in the systems with other solids, precipitation of magnesite first required nucleation of magnesite.

All nucleation processes require some extent of supersaturation in order to overcome the increase in

surface energy associated with forming a cluster of molecules. The free energy barrier for nucleation and the rate of nucleation are functions of the degree of supersaturation, temperature, and the interfacial free energy of the cluster–water interface. In the case of heterogeneous nucleation on an existing solid substrate, the interfacial energy of the cluster–substrate interface must also be considered (Lasaga, 1998; Stumm and Morgan, 1996). The nucleation rate can change by several orders of magnitude for relatively small changes in supersaturation, which contributes to the importance of a critical saturation ratio for nucleation. In the current work, critical supersaturation for magnesite nucleation occurred at a saturation index between 0.25 and 1.14, which corresponds to a Gibbs free energy difference from the equilibrium condition of 1800 to 8000 J mol<sup>-1</sup> at 95 °C. A study of calcite and magnesian calcite precipitation observed an induction period for homogeneous nucleation that increased as the extent of supersaturation decreased (Pokrovsky, 1998). An earlier study of magnesite precipitation at 126 °C in the presence of hydromagnesite found an induction period that decreased with increasing  $P_{\text{CO}_2}$  but was not a simple function of supersaturation (Sayles and Fyfe, 1973).

Heterogeneous nucleation on the surface of a substrate solid is energetically favorable if the interfacial free energy of the cluster–substrate interface is lower than that of the cluster–water interface (Lasaga, 1998; Stumm and Morgan, 1996). Although the presence of forsterite does not appear to significantly enhance magnesite precipitation relative to a solid-free system (Fig. 6b), magnesite nucleation and crystal growth are closely associated with the surfaces of forsterite particles, which suggests that the magnesite–forsterite interfacial free energy is lower than the magnesite–water interfacial free energy. However, the observations of similar overall magnesite precipitation in systems with and without forsterite and the three-dimensional growth of magnesite on forsterite suggest that the difference between the interfacial free energies of the magnesite–forsterite and magnesite–water interfaces must not be very large. If the difference in interfacial energies were larger, then minimization of the overall energy during magnesite precipitation would result in the formation of a thin film of magnesite, not

discrete three-dimensional precipitates. Heterogeneous nucleation and subsequent growth of magnesite has also been observed on hydromagnesite surfaces (Sayles and Fyfe, 1973).

The rate of crystal growth that follows nucleation is a function of the reactive surface area of the precipitate, pH, temperature, and reaction affinity. The surface area increases rapidly during the initial period of precipitation and the rate will increase proportionally. Fig. 5 illustrates this effect for magnesite precipitation in the presence of dissolving forsterite. If the dissolution–precipitation process is reversible, then Eq. (11) can also be used as a rate equation for precipitation; for supersaturated conditions  $\Delta G$  is positive and the negative dissolution rate that results is simply an indication that precipitation is occurring. Magnesite dissolution rate equations have been determined as functions of the magnesite surface speciation and Gibbs free energy change (Pokrovsky and Schott, 1999; Pokrovsky et al., 1999), and recent work has successfully applied those same equations and parameter values to magnesite precipitation (Oelkers et al., 2002). The rate equations of these previous studies were determined from steady-state conditions and can not be applied to the present work because precipitation of magnesite in the current experiments was never at steady state due to constantly changing surface area and solution pH.

#### 4.4. Implications for carbon storage and sequestration in deep saline aquifers

Mineral trapping involves the precipitation of solid mineral carbonate phases with carbon from injected CO<sub>2</sub>. Magnesite is likely to form in deep saline aquifers with sufficient sources of magnesium in either the initial brine or from the dissolution of Mg-containing silicate minerals. Although forsterite is uncommon in saline aquifers, it serves as a model for the release of Mg and neutralization of H<sub>2</sub>CO<sub>3</sub>\* that will occur during the dissolution of other Mg-containing silicates. The present work has implications for mineral trapping in saline aquifers and illustrates key parameters that affect mineral trapping.

Because the dissolution of silicate minerals provides a source of Mg for magnesite precipitation, the dissolution rates of silicate minerals at the

temperature, solution composition, and  $P_{\text{CO}_2}$  conditions of the aquifer must be known. Temperature and pH significantly affect dissolution rates. Temperature will vary with location according to the local geothermal gradient, and the 95 °C temperature is within the range of temperatures expected at the depths suggested for injection (Bachu, 2000). The pH of the aquifer will be governed by the interactions between the injected  $\text{CO}_2$  and the neutralizing capacity of the brine and aquifer minerals. Because the pH is strongly influenced by the dissolved  $\text{CO}_2$ , information on the solubility of  $\text{CO}_2$  as a function of temperature, pressure, and ionic strength is essential to determining dissolution rates. Fortunately, several recent studies have advanced the understanding of  $\text{CO}_2$  solubility at the conditions of interest (Blencoe et al., 2001a; Blencoe et al., 2001b; Duan and Sun, 2003; Enick and Klara, 1990; Rosenbauer and Koksalan, 2002; Seitz and Blencoe, 1999). The effects of ionic strength on  $\text{CO}_2$  solubility are particularly important for storage and sequestration in saline aquifers.

As Mg is released to solution and the injected  $\text{CO}_2$  is neutralized, the solution may become supersaturated with respect to magnesite. However, the presence of supersaturated conditions does not guarantee magnesite precipitation, and the kinetics of nucleation and crystal growth must also be considered. Nucleation requires that a critical degree of supersaturation be achieved. For magnesite at 95 °C and 100 bar  $P_{\text{CO}_2}$ , this critical supersaturation occurs at a saturation index between 0.25 and 1.14. Understanding the spatial and temporal variation of pH during deep saline aquifer  $\text{CO}_2$  storage and sequestration is important because pH influences both Mg-silicate dissolution and magnesite precipitation. While low pH facilitates Mg release to solution, high pH increases the magnesite saturation index, which facilitates magnesite nucleation and growth. As an illustration of the time required to reach initial and critical supersaturation, magnesite precipitation following forsterite dissolution can be calculated for some example conditions. For the rate of  $1.9 \times 10^{-13} \text{ mol cm}^{-2} \text{ s}^{-1}$  calculated earlier for 95°, 0.5 M ionic strength, and pH buffered at 5.65 (experiments P10–P12), a reactor containing 20 g  $\text{L}^{-1}$  of the 125–250  $\mu\text{m}$   $\text{Fo}_{89}$  will become supersaturated with respect to magnesite after 1.6 days and the critical supersatura-

tion will be reached after 2.8 to 22 days. The time required to reach saturation is highly dependent on the pH. While the dissolution rate of forsterite varies with  $\{\text{H}^+\}^{0.5}$ , the saturation index of magnesite depends upon  $\{\text{CO}_3^{2-}\}$  which varies with  $\{\text{H}^+\}^{-2}$  for systems in equilibrium with a fixed  $P_{\text{CO}_2}$ . For comparison with the values calculated at pH 5.65, times to reach initial and critical supersaturation can be determined for pH 4.65. The dissolution rate would be expected to increase from  $1.9 \times 10^{-13} \text{ mol cm}^{-2} \text{ s}^{-1}$  at pH 5.65 to  $6.0 \times 10^{-13} \text{ mol cm}^{-2} \text{ s}^{-1}$  at pH 4.65, but the time to reach initial saturation increases from 1.6 days to 26.5 days and the time to reach critical saturation becomes 47.2 to 363 days.

If the system initially contains magnesite, then the rate-limiting effects of nucleation are absent and mineral trapping by precipitation will occur sooner. Optimal aquifers for mineral trapping will be those containing large amounts of Mg-, Ca-, or Fe(II)-rich silicate minerals together with a small amount of pre-existing carbonate minerals that can act as seeds for crystal growth. In order to optimize mineral trapping, it may also be advantageous to add magnesite crystals as seeds for growth in conjunction with  $\text{CO}_2$  injection. The maintenance of supersaturated conditions and knowledge about critical saturation indices may enable control of the timing and location of carbonate precipitation as part of an injection management strategy. While magnesite and other carbonate minerals may nucleate on non-carbonate minerals, non-carbonate minerals may not substantially decrease the critical supersaturation required for magnesite nucleation.

The dissolution of silicate minerals and subsequent precipitation of carbonate minerals can also change bulk properties of the aquifer matrix. The volume changes associated with mineral dissolution and precipitation can alter the aquifer porosity and permeability in ways that may be beneficial or detrimental to an overall carbon storage and sequestration strategy. The volume change for the creation of 2 mol of magnesite and the consumption of one mole of forsterite is 12.2  $\text{cm}^3$ , which will decrease the porosity of the aquifer. The observations in the current work suggest that magnesite will precipitate as discrete particles, which will not limit subsequent silicate mineral dissolution. The effects of carbonate precipitation on silicate mineral dissolution and

aquifer porosity and permeability can be incorporated into reservoir simulations.

## 5. Conclusion

The extent of forsterite dissolution increased with both increasing  $P_{\text{CO}_2}$  and temperature. While the release of Mg and Si from forsterite was stoichiometric below the solubility limit of amorphous silica, the release of Fe was only stoichiometric at 30 °C. In unbuffered systems, the pH increased as carbonic acid was neutralized by the dissolution of forsterite. Dissolved concentrations of Mg and Si followed trajectories that ultimately intersect predicted equilibrium with magnesite and amorphous silica respectively. While observations suggested that amorphous silica precipitated, forsterite dissolution did not result in magnesite precipitation even though conditions of supersaturation were achieved.

Magnesite precipitation did occur when solution compositions were manipulated to reflect aqueous compositions that would result from extensive forsterite dissolution. Precipitation of magnesite was limited by the rate of magnesite nucleation. Nucleation required both sufficient time and a critical degree of supersaturation. At 95 °C the critical saturation index was between 0.25 and 1.14. When the limitation of magnesite nucleation was avoided by seeding reactors with magnesite, the precipitation rate was more rapid than in systems without magnesite. In systems seeded with forsterite, magnesite nucleation appeared to occur heterogeneously with the precipitation of magnesite crystals on the surfaces of forsterite particles; however, the presence of forsterite did not significantly accelerate magnesite nucleation relative to solid-free systems.

The results of the present work emphasize the importance of  $P_{\text{CO}_2}$  and temperature on the reactions that will occur between aquifer minerals, brine, and  $\text{CO}_2$  following  $\text{CO}_2$  injection into deep saline aquifers. The high solid–water ratios in aquifers may facilitate carbonate mineral precipitation, and the presence of pre-existing carbonate minerals would accelerate mineral trapping reactions. The importance of the degree of saturation on nucleation and precipitation rates may offer a means of influencing the timing and location of carbonate mineral precipitation, which may be benefi-

cial to controlling the bulk hydrogeologic properties of a receiving aquifer system.

While the study of forsterite has implications for the dissolution of other silicate minerals, more research needs to be done to investigate the reactions of common aquifer and aquitard minerals at the high temperature,  $P_{\text{CO}_2}$ , and ionic strength conditions of deep saline aquifers. Subsequent work should also expand the range of conditions, especially pH, which may offer insights into additional effects of  $\text{CO}_2$ , including the carbonate ion-mediated inhibition or enhancement of mineral dissolution at higher pH.

## Acknowledgments

This work was performed as part of the Carbon Mitigation Initiative (CMI) in the Princeton Environmental Institute. The CMI is sponsored by BP and The Ford Motor Company. Sean Shieh, Jane Woodruff, and Maria Borcsik each provided valuable analytical assistance. While at Princeton, Daniel Giammar's fellowship was supported by the Princeton Council on Science and Technology and the Department of Geosciences. Dr. Giammar is grateful for this support and also wishes to acknowledge Satish Myneni for his mentorship and support. We appreciate the critical and insightful comments of Eric Oelkers, Michael Hodson, and Oleg Pokrovsky in their reviews of the manuscript. [EO]

## References

- Albritton, D.L., Meira Filho, L.G., 2001. Technical summary. In: Houghton, J.T., et al., (Eds.), *Climate Change 2001: The Scientific Basis; Contribution of Working Group I to the Third Assessment Report to the Intergovernmental Panel on Climate Change*. Cambridge University Press, Cambridge, United Kingdom, pp. 21–83.
- Bachu, S., 2000. Sequestration of  $\text{CO}_2$  in geological media: criteria and approach for site selection in response to climate change. *Energy Convers. Manag.* 41, 953–970.
- Bachu, S., Gunter, W.D., Perkins, E.H., 1996. Carbon dioxide disposal. In: Hitchon, B. (Ed.), *Aquifer Disposal of Carbon Dioxide. Hydrodynamic and Mineral Trapping—Proof of Concept*. Geoscience Publishing Ltd., Sherwood Park, Alberta, Canada, pp. 11–22.
- Batzle, M., Wang, Z.J., 1992. Seismic properties of pore fluids. *Geophysics* 57 (11), 1396–1408.

- Berg, A., Banwart, S.A., 2000. Carbon dioxide mediated dissolution of Ca-feldspar: implications for silicate weathering. *Chem. Geol.* 163 (1–4), 25–42.
- Blencoe, J.G., Cole, D.R., Horita, J., Moline, G., 2001a. Experimental geochemical studies relevant to carbon sequestration. First National Conference on Carbon Sequestration. National Energy Technology Laboratory, Washington, DC. [www.netl.doe.gov/publications/proceedings/01/carbon\\_seq/p31.pdf](http://www.netl.doe.gov/publications/proceedings/01/carbon_seq/p31.pdf).
- Blencoe, J.G., Naney, M.T., Anovitz, L.M., 2001b. The CO<sub>2</sub>–H<sub>2</sub>O system: III. A new experimental method for determining liquid–vapor equilibria at high subcritical temperatures. *Am. Mineral.* 86 (9), 1100–1111.
- Blum, A., Lasaga, A.C., 1988. Role of surface speciation in the low-temperature dissolution of minerals. *Nature* 331 (4), 431–433.
- Brady, P.V., Carroll, S.A., 1994. Direct effects of CO<sub>2</sub> and temperature on silicate weathering: possible implications for climate control. *Geochim. Cosmochim. Acta* 58 (8), 1853–1856.
- Brantley, S.L., Mellott, N.P., 2000. Surface area and porosity of primary silicate minerals. *Am. Mineral.* 85, 1767–1783.
- Bruant Jr., R.G., Celia, M.A., Guswa, A.J., Peters, C.A., 2002. Safe storage of CO<sub>2</sub> in deep saline aquifers. *Environ. Sci. Technol.* 36 (11), 240A–245A.
- Brunauer, S., Emmett, P.H., Teller, E., 1938. Adsorption of gases in multimolecular layers. *J. Am. Chem. Soc.* 60, 309–319.
- Carroll, S.A., Knauss, K.G., 2001. Experimental determination of Ca-silicate dissolution rates: a source of calcium for geologic CO<sub>2</sub> sequestration. First National Conference on Carbon Sequestration. National Energy Technology Laboratory, Washington, DC. [http://www.netl.doe.gov/publications/proceedings/01/carbon\\_seq/p27.pdf](http://www.netl.doe.gov/publications/proceedings/01/carbon_seq/p27.pdf).
- Casey, W.H., Westrich, H.R., 1992. Control of dissolution rates of orthosilicate minerals by divalent metal–oxygen bonds. *Nature* 355, 157–159.
- Chen, Y., Brantley, S.L., 2000. Dissolution of forsteritic olivine at 65 °C and 2 < pH < 5. *Chem. Geol.* 165, 267–281.
- Davies, C.W., 1962. *Ion Association*. Butterworths, Washington, DC.
- Duan, Z., Sun, R., 2003. An improved model calculating CO<sub>2</sub> solubility in pure water and aqueous NaCl solutions from 273 to 533 K and from 0 to 2000 bar. *Chem. Geol.* 193, 257–271.
- Enick, R.M., Klara, S.M., 1990. CO<sub>2</sub> solubility in water and brine under reservoir conditions. *Chem. Eng. Commun.* 90, 23–33.
- Goff, F., Lackner, K.S., 1998. Carbon dioxide sequestering using ultramafic rocks. *Environ. Geosci.* 5 (3), 89.
- Gunter, W.D., Wiwchar, B., Perkins, E.H., 1996. Autoclave experiments and geochemical modelling. In: Hitchon, B. (Ed.), *Aquifer Disposal of Carbon Dioxide. Hydrodynamic and Mineral Trapping—Proof of Concept*. Geoscience Publishing Ltd., Sherwood Park, Alberta, Canada, pp. 115–141.
- Gunter, W.D., Perkins, E.H., Hutcheon, I., 2000. Aquifer disposal of acid gases: modelling of water–rock reactions for trapping of acid wastes. *Appl. Geochem.* 15, 1085–1095.
- Guthrie Jr., G.D., Carey, J.W., Bergfeld, D., Byler, D., Chipera, S., Zioc, H.-J., et al., 2001. Geochemical aspects of the carbonation of magnesium silicates in an aqueous medium. First National Conference on Carbon Sequestration. National Energy Technology Laboratory, Washington, DC. [www.netl.doe.gov/publications/proceedings/01/carbon\\_seq/6c4.pdf](http://www.netl.doe.gov/publications/proceedings/01/carbon_seq/6c4.pdf).
- Hodson, M.E., 2003. The influence of Fe-rich coatings on the dissolution of anorthite at pH 2.6. *Geochim. Cosmochim. Acta* 67 (18), 3355–3363.
- Johnson, J.W., Oelkers, E.H., Helgeson, H.C., 1992. SUPCRT92: a software package for calculating the standard molal thermodynamic properties of minerals, gases, aqueous species and reactions from 1 to 5000 bar and 0 to 1000 °C. *Comput. Geosci.* 18 (7), 899–947.
- Johnson, J.W., Nitao, J.J., Steefel, C.I., Knauss, K.G., 2001. Reactive transport modeling of geologic CO<sub>2</sub> sequestration in saline aquifers: the influence of intra-aquifer shales and the relative effectiveness of structural, solubility, and mineral trapping during prograde and retrograde sequestration. First National Conference on Carbon Sequestration. National Energy Technology Laboratory, Washington, DC. [www.netl.doe.gov/publications/proceedings/01/carbon\\_seq/P28.pdf](http://www.netl.doe.gov/publications/proceedings/01/carbon_seq/P28.pdf).
- Johnson, J.W., Nitao, J.J., Steefel, C.I., 2002. Fundamental elements of geologic CO<sub>2</sub> sequestration in saline aquifers, 223rd American Chemical Society National Meeting, ACS Fuel Chemistry Division Symposia Preprints. American Chemical Society, Orlando, Florida, pp. 41–42.
- Kaszuba, J.P., Janecky, D.R., Snow, M.G., 2003. Carbon dioxide reaction processes in a model brine aquifer at 200 °C and 200 bars: implications for geologic sequestration of carbon. *Appl. Geochem.* 18, 1065–1080.
- Knauss, K.G., Nguyen, S.N., Weed, H.C., 1993. Diopside dissolution kinetics as a function of pH, CO<sub>2</sub>, temperature, and time. *Geochim. Cosmochim. Acta* 57 (2), 285–294.
- Kump, L.R., Brantley, S.L., Arthur, M.A., 2000. Chemical weathering, atmospheric CO<sub>2</sub>, and climate. *Annu. Rev. Earth Planet. Sci.* 28, 611–667.
- Lasaga, A.C., 1995. Fundamental approaches in describing mineral dissolution and precipitation rates. In: White, A.F., Brantley, S.L. (Eds.), *Chemical Weathering Rates of Silicate Minerals. Reviews in Mineralogy*. Mineralogical Society of America, Washington, D.C., pp. 23–86.
- Lasaga, A.C., 1998. *Kinetic Theory in the Earth Sciences*. Princeton Series in Geochemistry. Princeton University Press, Princeton, New Jersey. 811 pp.
- Luce, R.W., Bartlett, R.W., Parks, G.A., 1972. Dissolution kinetics of magnesium silicates. *Geochim. Cosmochim. Acta* 36, 35–50.
- O'Connor, W.K., Dahlin, D.C., Rush, G.E., Dahlin, C.L., Collins, W.K., 2002. Carbon dioxide sequestration by direct mineral carbonation: process mineralogy of feed and products. *Miner. Metall. Process.* 19 (2), 95–101.
- Oelkers, E.H., 2001. An experimental study of forsterite dissolution rates as a function of temperature and aqueous Mg and Si concentrations. *Chem. Geol.* 175, 485–494.
- Oelkers, E.H., Pokrovsky, O.S., Schott, J., 2002. An experimental study of magnesite dissolution and precipitation rates. Geological Society of America Annual Meeting. GSA, Denver, Colorado.
- Pokrovsky, O.S., 1998. Precipitation of calcium and magnesium carbonates from homogeneous supersaturated solutions. *J. Cryst. Growth* 186 (1–2), 233–239.
- Pokrovsky, O.S., Schott, J., 1999. Processes at the magnesium-bearing carbonates solution interface: II. Kinetics and mecha-

- nism of magnesite dissolution. *Geochim. Cosmochim. Acta* 63 (6), 881–897.
- Pokrovsky, O.S., Schott, J., 2000a. Forsterite surface composition in aqueous solutions: a combined potentiometric, electrokinetic, and spectroscopic approach. *Geochim. Cosmochim. Acta* 64 (19), 3299–3312.
- Pokrovsky, O.S., Schott, J., 2000b. Kinetics and mechanism of forsterite dissolution at 25 °C and pH from 1 to 12. *Geochim. Cosmochim. Acta* 64 (19), 3313–3325.
- Pokrovsky, O.S., Schott, J., Thomas, F., 1999. Processes at the magnesium-bearing carbonates solution interface: I. A surface speciation model for magnesite. *Geochim. Cosmochim. Acta* 63 (6), 863–880.
- Press, F., Siever, R., 1998. *Understanding Earth*. W. H. Freeman and Company, New York, New York.
- Rodrigues, E., El Amrani, F.Z., Giménez, J., Casas, I., Torroero, M.E., de Pablo, J., et al., 1998. Surface characterization of olivine-rock by X-ray photoelectron spectroscopy (XPS), leaching and U(VI)-sorption experiments, *Materials Research Society*. Materials Research Society, pp. 321–327.
- Rosenbauer, R.J., Koksalan, T., 2002. Experimental determination of the solubility of CO<sub>2</sub> in electrolytes: application to CO<sub>2</sub> sequestration in deep-saline aquifers. Geological society of America Annual Meeting. GSA, Denver, Colorado.
- Rosso, J.J., Rimstidt, J.D., 2000. A high resolution study of forsterite dissolution rates. *Geochim. Cosmochim. Acta* 64 (5), 797–811.
- Sass, B.M., Gupta, N., Ickes, J.A., Engelhard, M.H., Baer, D.R., Bergman, P., et al., 2001. Interactions of rock minerals with carbon dioxide and brine: a hydrothermal investigation. First National Conference on Carbon Sequestration. National Energy Technology Laboratory, Washington, DC. [www.netl.doe.gov/publications/proceedings/01/carbon\\_seq/4a4.pdf](http://www.netl.doe.gov/publications/proceedings/01/carbon_seq/4a4.pdf).
- Sayles, F.L., Fyfe, W.S., 1973. The crystallization of magnesite from aqueous solution. *Geochim. Cosmochim. Acta* 37, 87–99.
- Schecher, W.D., McAvoy, D.C., 1998. MINEQL+: A Chemical Equilibrium Modeling System, Version 4.5. Environmental Research Software, Hallowell, ME.
- Seitz, J.C., Blencoe, J.G., 1999. The CO<sub>2</sub>–H<sub>2</sub>O system: I. Experimental determination of volumetric properties at 400 °C, 10–100 MPa. *Geochim. Cosmochim. Acta* 63 (10), 1559–1569.
- Seyama, H., Soma, M., Tanaka, A., 1996. Surface characterization of acid-leached olivines by X-ray photoelectron spectroscopy. *Chem. Geol.* 129, 209–216.
- Stephens, J.C., 2002. Response of soil mineral weathering to elevated carbon dioxide. Doctoral thesis, California Institute of Technology, Pasadena, California.
- Stephens, J.C., Hering, J.G., 2004. Factors affecting the dissolution kinetics of volcanic ash soils: dependencies on pH, CO<sub>2</sub>, and oxalate. *Appl. Geochem.* 19 (8), 1217–1232.
- Sterner, M.S., Pitzer, K.S., 1994. An equation of state for carbon dioxide valid from zero to extreme pressures. *Contrib. Mineral. Petrol.* 117, 362–374.
- Stumm, W., Morgan, J.J., 1996. *Aquatic Chemistry*. John Wiley & Sons Inc., New York, NY.
- Westrich, H.R., Cygan, R.T., Casey, W.H., Zemitis, C., Arnold, G.W., 1993. The dissolution kinetics of mixed-cation orthosilicate minerals. *Am. J. Sci.* 293 (9), 869–893.
- Wogelius, R.A., Walther, J.V., 1991. Olivine dissolution at 25 °C: effects of pH, CO<sub>2</sub>, and organic acids. *Geochim. Cosmochim. Acta* 55 (4), 943–954.
- Wogelius, R.A., Walther, J.V., 1992. Olivine dissolution kinetics at near-surface conditions. *Chem. Geol.* 97, 101–112.
- Xu, T., Apps, J.A., Pruess, K., 2001. Analysis of Mineral Trapping for CO<sub>2</sub> Disposal in Deep Aquifers. LBNL-46992, Lawrence Berkeley National Laboratory, Berkeley, California.